

¹ A simulation model of front-end electronics for high-precision
² timing measurements with low-gain avalanche detectors.

³ C. Peña^{*,a,b}, G. Deptuch^a, S. Xie^b, A. Apresyan^a, L. Narvaez^b, T. Liu^a, N. Cartiglia^c

⁴ *^aFermi National Accelerator Laboratory, Batavia, IL, USA*

⁵ *^bCalifornia Institute of Technology, Pasadena, CA, USA*

⁶ *^cINFN, Torino, Italy*

⁷ **Abstract**

In this paper we report simulation results of a study aiming to optimize some parameters of a detector that uses low-gain avalanche detectors (LGAD) for high-precision timing measurements. The detector is assumed to be composed of a 50 μm LGAD sensor connected to a front-end electronics which is used to measure the time of arrival of minimum ionizing particles. The simulation includes modeling of signal fluctuations in LGAD, variations of the analog bandwidth and signal-to-noise ratio of the front-end electronics, time quantization (time-to-digital converter resolution), and effects of radiation damage on LGAD signals. Two approaches to measure the timestamp are considered: leading edge and constant fraction. Additionally, the time resolution is studied as function of the level of irradiation of the sensor. Simulated LGAD pulses before irradiation, and after neutron fluences of $5 \times 10^{14} \text{ n/cm}^2$ and $1 \times 10^{15} \text{ n/cm}^2$, are studied. The time resolution for a 50 μm LGAD was found to be 35 ps for front-end electronics bandwidths larger than 350 MHz and SNRs larger than 30. The time resolution at a SNR of 30 for fluences of $5 \times 10^{14} \text{ n/cm}^2$ and $1 \times 10^{15} \text{ n/cm}^2$ were found to be 31 ps and 37 ps, respectively.

⁸ *Key words:*

⁹ Silicon, Timing, LGAD

¹⁰ **Contents**

¹¹ 1 Introduction	²
¹² 2 Simulation Framework	²
2.1 Front-end electronics and noise injection	3
2.1.1 Front-end simulation	5
2.1.2 Noise injection	5

*Corresponding author

Email address: cmorgoth@fnal.gov (C. Peña)

16	3 Timing Reconstruction and Analysis	6
17	3.1 Leading edge and constant fraction discriminators	7
18	3.1.1 constant fraction discriminator implementations	7
19	3.2 Time-walk correction and time-over-threshold	7
20	4 LGAD Front-end Electronics Performance	9
21	4.1 Front-end electronics shaping time and SNR studies	9
22	4.2 Timing performance as a function of irradiation	10
23	5 Conclusion	11

24 **1. Introduction**

25 Low-gain avalanche diodes (LGAD) are envisioned to be used in the CMS and AT-
 26 LAS experiment upgrades for HL-LHC in order to overcome the event reconstruction
 27 challenges posed by the high rate of concurrent collisions per beam crossing (pileup).
 28 The implemented regions of pseudorapidity (η) are: $1.6 < |\eta| < 2.9$, and $2.4 < |\eta| < 4.2$
 29 for CMS and ATLAS, respectively. Beam test measurements have demonstrated that
 30 the required time resolution, radiation tolerance, and uniformity of LGAD sensors can
 31 be achieved [1].

32 In this paper we report simulation results of a study aiming to optimize some parame-
 33 ters of a detector that uses 50 μm low-gain avalanche detectors (LGAD) for high-precision
 34 timing measurements. The simulation model includes effects due to variations in LGAD
 35 signal pulse shape and amplitude, different analog bandwidth and signal-to-noise ratio
 36 of the front-end electronics, time quantization (time-to-digital converter resolution), and
 37 effects of radiation damage on LGAD signals. We scan the important parameters for
 38 timing resolution: analog bandwidths (BWs), signal-to-noise ratios (SNR), and the total
 39 fluence that the LGAD sensor has been subjected to. Our results indicate that for FEE
 40 analog BWs larger than 350 MHz, corresponding to shaping times less than 1 ns and
 41 SNR larger than 30, time resolutions of 30–37 ps and 34–47 ps are obtained when using
 42 constant fraction (CF) and leading edge (LE) discriminators, respectively. These results
 43 are compatible with previous measurements on LGAD timing resolutions carried out
 44 under laboratory and beam test conditions [1–3]. We study the time resolution of four
 45 different FEE shaping times: 0.5 ps, 1.0 ps, 2.0 ps, and 4.0 ps; three SNR: 20, 30, 100;
 46 and three sensor irradiation levels: pre-radiation, $5 \times 10^{14} \text{ n/cm}^2$, and $1 \times 10^{15} \text{ n/cm}^2$.
 47 For every point in this scan we evaluate the time resolution for LE and CF. Our results
 48 are a guideline on what time resolution can be achieved for a particular combination of
 49 analog bandwidth, SNR, and sensor.

50 The paper is organized as follows: the simulation is described in Sec. 2; algorithms
 51 used in the timing reconstruction and analysis are described in Sec. 3; simulation results
 52 are presented in Sec. 4, followed by the conclusion in Sec. 5.

53 **2. Simulation Framework**

54 Unprocessed signal pulses from the LGAD sensors are obtained from Weightfield2
 55 (WF2), a 2-dimensional silicon simulator [4]. WF2 was used to simulate sets of 1000
 56 signal pulses modeling the response off minimum-ionizing particles (MIP) traversing the

57 LGAD sensor, and the MIP impinges on the LGAD perpendicularly to its surface. Three
 58 sets of such signal pulses were generated for a $50 \mu\text{m}$ LGAD sensor at different levels
 59 of sensor irradiation: pre-irradiation, and after neutron fluences of $5 \times 10^{14} \text{n/cm}^2$ and
 60 $1 \times 10^{15} \text{n/cm}^2$. Fig. 1 shows the LGAD output current (unprocessed signal pulses)
 61 from WF2 for 1000 pulses (left) and example pulses for all the irradiation levels studied
 62 (right). Gaussian white noise is added to these unprocessed signals, and the combined
 63 waveform is fed into the simulation of the FEE. The schematic diagram of the data flow
 64 of is illustrated in Fig. 3 and described in further detail in Sec. 2.1. The output of the
 65 FEE simulation is the convolution of the impulse response function and the input signal
 66 at the FEE. We consider four shaping constants for the impulse response of the FEE:
 67 0.5, 1.0, 2.0, and 4.0 ns. At the output of the FEE block, we obtain simulated processed
 68 LGAD pulses, which include the effects of sensor fluctuations, the shaping of the FEE,
 69 and noise. The resulting processed pulses are scaled such that the most probable value
 70 (MPV) for each of the simulated conditions is 50 mV. This choice of normalization does
 71 not affect the time resolution results since the SNR is maintained. By enforcing the same
 72 normalization for every simulation condition we ensure that the LE thresholds don't have
 73 to be retuned.

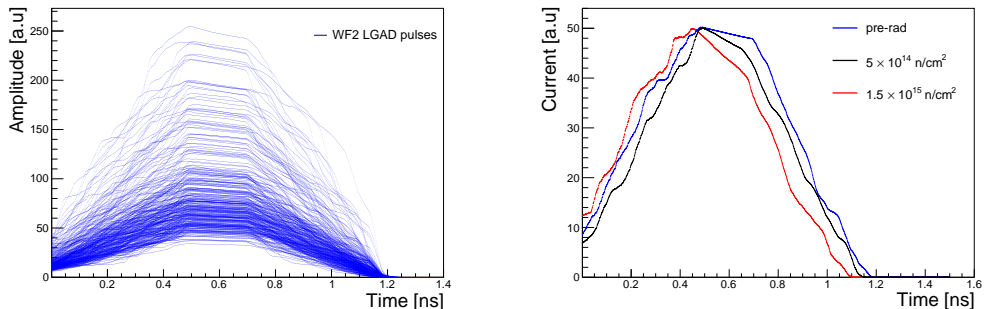


Figure 1: (Left) One thousand LGAD output current pulse from WF2 for a pre-radiation sensor. (Right) example LGAD output current pulse for different irradiation levels, legend is shown in the plot.

74 A waveform analysis is performed with the pulses obtained at the output of the FEE
 75 block. We assign timestamps to each pulse by using algorithms that emulate ideal LE
 76 and CF discriminators. For each threshold we obtain an LE and CF timestamp as well
 77 as the corresponding time-over-threshold (ToT) of the pulse. The SNR is defined as the
 78 ratio of the MPV of the amplitude distribution to the r.m.s of the amplitude distribution
 79 at a fixed sample of noise-only waveforms. Fig. 2 shows the amplitude distribution and
 80 the respective Landau fit from where the MPV is obtained (left) and the amplitude
 81 distribution for a fixed sample (right) for a pre-radiation sensor with a SNR of 30. We
 82 study three SNR scenarios: 20, 30, and 100. A schematic diagram of the simulation is
 83 shown in Fig. 3.

84 2.1. Front-end electronics and noise injection

85 The front-end simulation combines analytical calculations and numerical methods.
 86 We implement two independent simulations, one based on the time domain and the
 87 other on the Laplace domain. Both simulation use the unprocessed WF2 LGAD pulses

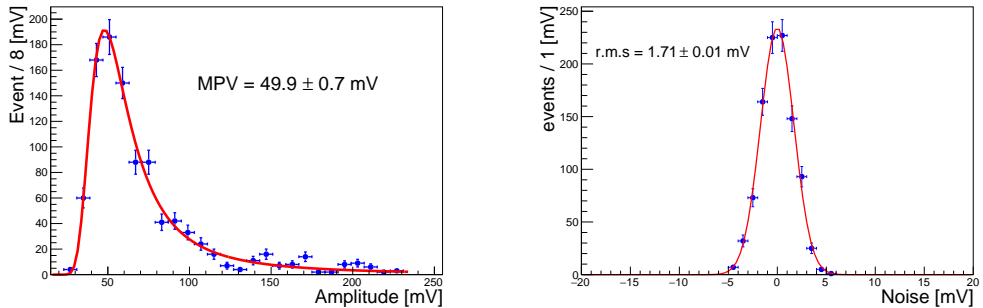


Figure 2: (Left) Amplitude distribution after the FEE. A Landau fit is performed to obtain the MPV. (Right) Amplitude distribution at a fixed sample of noise-only waveforms. A gaussian fit performed to obtain the r.m.s. Both figures correspond to a pre-radiation sensor using a shaping time (ST) of 1 ns and a SNR of 30.

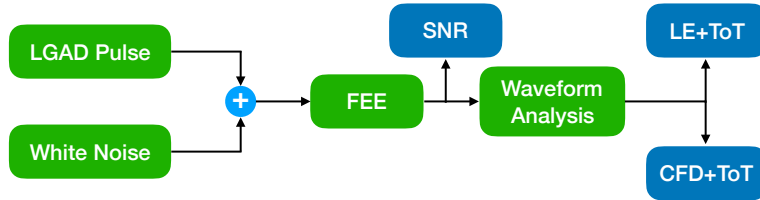


Figure 3: A schematic diagram of the simulation. Each simulation configurable block is shown in green. The most relevant outputs of the simulation are shown in blue.

88 as input (see Fig 1). The results of the two simulations are in agreement within statistical
 89 uncertainties and provide a cross check of the results. Sections 2.1.1 and 2.1.2 describe
 90 the details of the implementation of the front-end and noise simulation.

91 *2.1.1. Front-end simulation*

92 The front-end simulation is based on a single amplification stage. We focus on the
 93 BW of such an amplifier rather than variations thereof. The FEE is a second order low-
 94 pass filter with transfer function ($H(S)$) and impulse response ($h(t)$) given by equations 1
 95 and 2, respectively.

$$96 \quad H(S) = \frac{\frac{1}{\tau_s^2}}{(S + 1/\tau_s)^2} \quad (1) \qquad h(t) = \frac{t}{\tau_s^2} e^{-t/\tau_s} \quad (2)$$

97 The output pulse of the FEE is the convolution (in time domain) of the unprocessed
 98 LGAD signal pulse from WF2 and the FEE impulse response function, given in Eq. 2.
 99 The sampling time for the pulses and the convolution is 10 ps, this choice is used through-
 100 out the simulation. As stated above we focus the study on the BW of the FEE and to
 101 that end we scan the τ_s parameter in Eq. 2 in the following set: $\{0.5, 1, 2, 4\}$ ns. This
 102 parameter is hereafter referred to as shaping time (ST). Figure 4 (left) shows the com-
 103 parison of the impulse and LGAD responses for a ST of 1 ns while Figure 4 (right) shows
 104 the LGAD response for all STs studied. We observe that the LGAD response is delayed
 105 with respect to the impulse response, and that pulse slew rate is decreased in the first
 106 nanosecond of the pulse. As expected, we also observe that the pulse risetime scale up
 107 with the ST and that the decay time is dominated by the ST. We define rise time as
 108 the time required for the signal to rise from 10% to 90% of its amplitude, and Tab. 2.1.1
 109 shows the set of ST and risetimes that we studied.

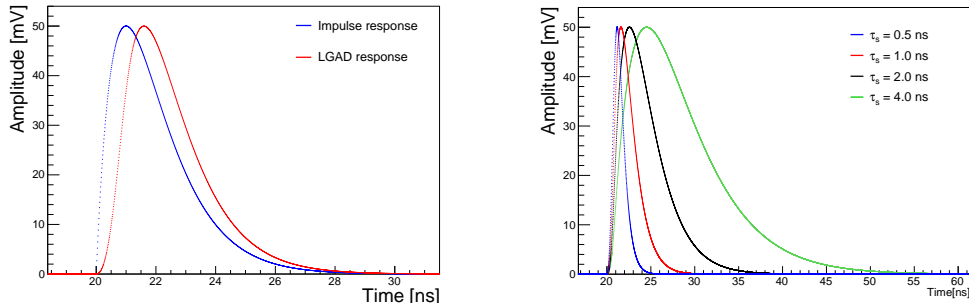


Figure 4: (Left) Comparison of impulse and LGAD responses for a shaping time (ST) of 1 ns. (Right) LGAD response for the four shaping times studied: $\{0.5, 1, 2, 4\}$ ns. All pulses have been normalized to achieve a peak amplitude of 50 mV. Legends for the shaping times are shown in the plots.

110 *2.1.2. Noise injection*

111 Gaussian white noise is simulated by sampling every 10 ps. Each sampled time is
 112 assigned a random amplitude which is drawn from a gaussian distribution with zero mean
 113 and width corresponding to the SNR under study. It is important to note that the width

ST (ns)	0.5	1.0	2.0	4.0
Risetime (ns)	0.67 ± 0.02	0.86 ± 0.02	1.36 ± 0.02	2.48 ± 0.02

Table 1: Measured risetime for all shaping times studied: $\{0.5, 1, 2, 4\}$ ns. The uncertainty is the r.m.s of the risetime distribution.

of the gaussian parameter is not exactly the SNR and needs to be adjusted depending on the ST of the FEE. The left panel of Figure 5 shows the gaussian white noise before and after a 1 ns FEE. We see a clear shaping in the time structure of the noise. We checked that the average noise power spectrum is flat in the frequency domain up to at least 10 GHz. We observe the expected $\sqrt{(\text{BW})}$ scaling of the noise after the FEE for all the STs under study. The right panel of Figure 5 shows the output of the FEE block, with a 1 ns ST, for a pre-irradiated LGAD pulse after noise has been injected. The injected noise is such that the SNR is 30. SNR is defined as the ratio of the most probable value (MPV) of the pulse height distribution to the the r.m.s of the 100th sample, over an ensemble of 1000 pulses.

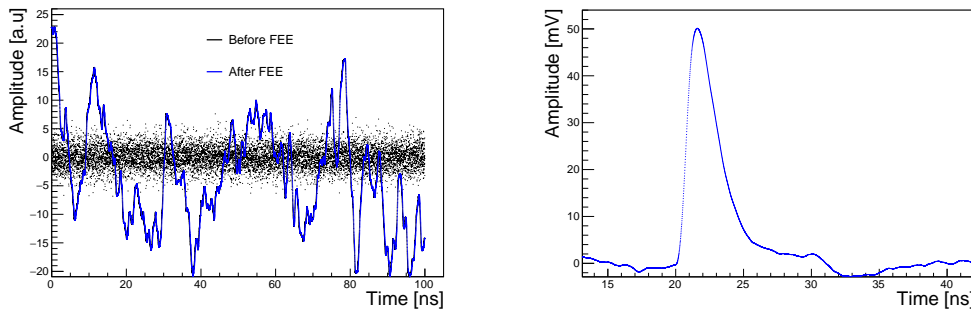


Figure 5: (Left) Comparison of gaussian white noise before and after the FEE, legend is shown in plot. (Right) Example pulse at the output of the FEE block with a SNR of 30. Both figure use a shaping time (ST) of 1 ns.

3. Timing Reconstruction and Analysis

The time reconstruction is based on waveform analysis. We generate an ensemble of 1000 pulses sampled every 10 ps. Each pulse is interpolated using the Whittaker-Shannon formula [5, 6]

$$f(t) = \sum f(kT) \frac{\sin(\pi(t/T - k))}{\pi(t/T - k)}. \quad (3)$$

Where f is pulse we want to interpolate, t is the continuous time variable, $k = 0, \pm 1, \pm 2, \dots$, and T is the sampling time (10 ps). Using the interpolated pulse we assign a timestamp by finding when a given voltage threshold has been crossed. The threshold can be a constant value (LE) or a constant fraction of the pulse height (CF). In the case of the CFD we also simulate more realistic implementations: [split-and-delay as well as as second order RC filter \(Greg, please check naming\)](#). More details about the algorithms

134 are given in Sec. 3.1. The time resolution is estimated by the width parameter of a
135 gaussian fit to the timestamps obtained for a particular threshold. We apply a time-walk
136 correction based on the time-over-threshold of the pulse. We note that this correction
137 has a large improvement on the time resolution measured using the LE algorithm while
138 the CF algorithm is mostly insensitive to this correction, as seen in Fig. 6. Details about
139 this correction are covered in Sec. 3.2. We scan the LE and CF threshold such that we
140 find the one with the best time resolution.

141 *3.1. Leading edge and constant fraction discriminators*

142 The leading edge and constant fraction discriminator algorithms are *ideal* in the
143 sense that they don't simulate the effect of electronics in a real implementation. Our
144 approach is to sample the pulses every 10 ps and subsequently interpolate them using
145 the Whittaker-Shannon formula ($\sin(x)/x$) to more accurately determine the threshold
146 crossing. In the LE case the threshold is scanned from 3–60 mV, while the CFD is
147 scanned from 5–90 % of the current pulse maximum amplitude. For each threshold we
148 obtain two timestamps: when the pulse first crosses the threshold (t_0) and when it crosses
149 the second time (t_1), now in the opposite direction. The time-over-threshold is defined
150 as the difference of the two timestamps ($ToT = t_1 - t_0$). The first timestamp, t_0 , is used
151 to determine the time resolution at given threshold. The time resolution is defined as
152 the width of a gaussian fit to the t_0 distribution binned with a bin-width of 20 ps. The
153 time resolution is obtained in two cases: before and after a time-walk correction. The
154 time-walk correction aims to correct the known effect of time drift as a function of the
155 pulse height. The time-walk correction removes this time drift and ensures that the time
156 response is flat as a function of the pulse height. Figure 6 shows the time resolution as
157 a function of the threshold required for a pre-irradiated LGAD sensor with a ST of 1 ns
158 and a SNR of 30. Fig. 7 shows a typical t_0 distribution, using the LE and CF algorithms,
159 for the pre-irradiated LGAD sensor after the ToT correction has been applied. The time
160 resolution (σ_t) is measured to be 37.3 ± 1.4 and 33.0 ± 1.4 for the LE and CF, respectively.
161 Additionally, we study more *realistic* CFD implementations: **split-and-delay as well as a**
162 **second order RC filter (Greg, please check naming)** (see Sec. 3.1.1). We observe that *ideal*
163 and split-and delay CFD implementations yield equivalent results within uncertainties.
164 The second order RC filter shows a degradation on performance with respect to the
165 split-and-delay implementation.

166 *3.1.1. constant fraction discriminator implementations*

167 GREG: PLEASE ADD TEXT HERE, I called the two implementations split-and-
168 delay and second order RC previously in the text (also in red).

169 *3.2. Time-walk correction and time-over-threshold*

170 A time-walk correction is applied in order to correct the timestamp drift of pulses
171 with varying amplitudes. The correction is based on the measured time-over-threshold:
172 $ToT = t_1 - t_0$. As expected, we observe that the ToT correction is large for the LE case
173 and negligible for CF (see Fig. 6). Figure 8 (left) shows a typical two dimensional map
174 of t_0 and ToT for the LE algorithm, wherein a clear correlation between t_0 and ToT is
175 observed. The time-walk correction is obtain by measuring the average t_0 in each ToT
176 bin and subsequently fitting a 2nd-order polynomial (see Fig. 8 (right)). The resulting

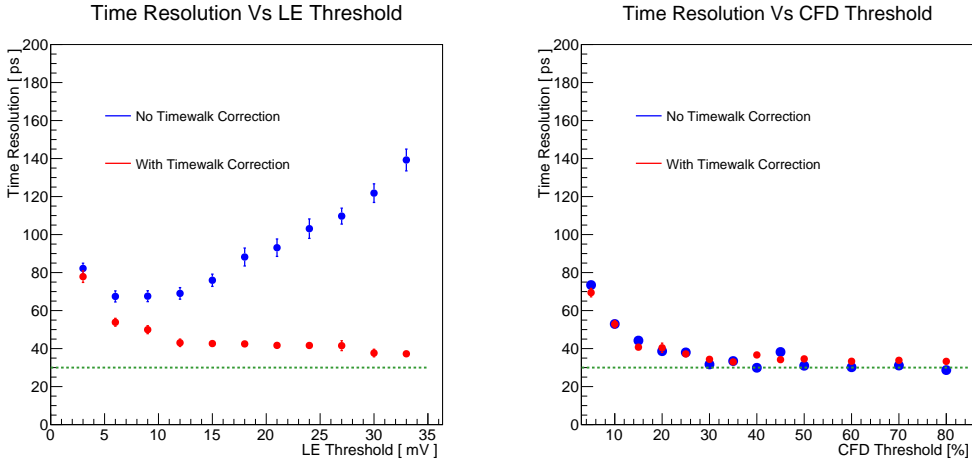


Figure 6: (Left) LE time resolution as a function of threshold. (Right) CF time resolution as a function of threshold. Both figure use pre-irradiated LGAD sensor with a ST of 1 ns and a SNR of 30.

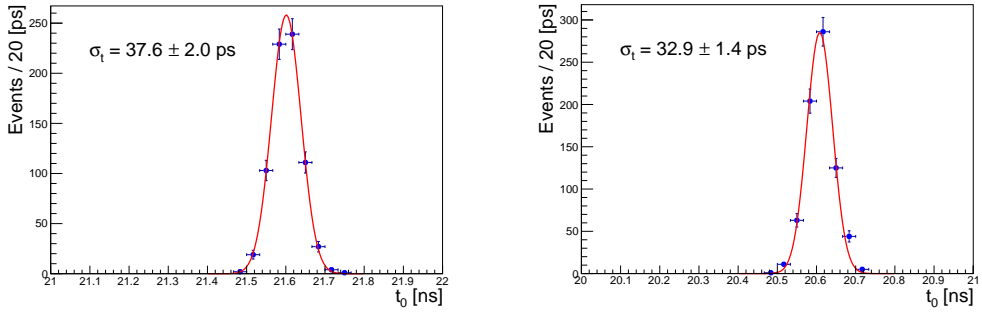


Figure 7: (Left) timestamp (t_0) distribution for a 30 mV threshold using a leading edge discriminator. (Right) timestamp (t_0) distribution for a 35% threshold using a constant fraction discriminator. Both figures include the time-walk correction based on the measured ToT. Both figures use pre-irradiated unprocessed pulses, a shaping time (ST) of 1 ns, and correspond to SNR of 30.

177 analytical expression after the fit is then used to correct and flatten the dependence of t_0
 178 on ToT. The time-walk correction is expressed in Eq. 4, where p_2 and p_1 are the quadratic
 179 and linear coefficients of the 2nd-order polynomial fit. Different corrections are derived for
 180 each simulation scenario characterized by the values of the simulation parameters: ST,
 181 SNR, and LGAD irradiation level. As shown in Fig. 6 (left) the effect of the time-walk
 182 depends on the threshold used and correcting for it can yield significant improvements
 183 in the measured time resolution.

$$t_0 = t_0 - (p_2 \text{ToT}^2 + p_1 \text{ToT}) \quad (4)$$

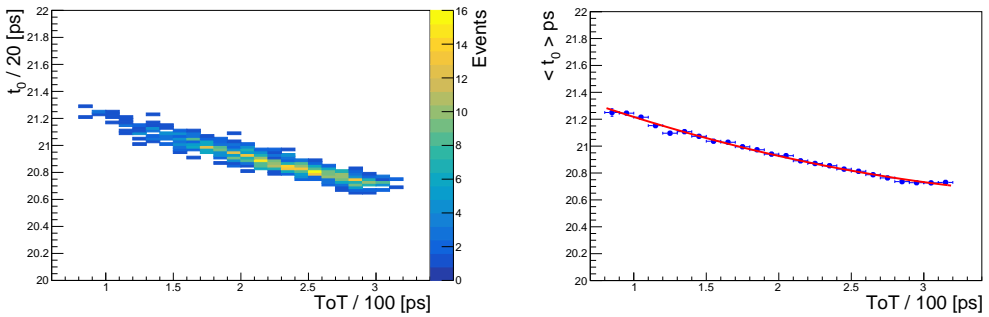


Figure 8: (Left) two dimensional map of the timestamp (t_0) and ToT ($t_1 - t_0$). (Right) one dimensional projection of the timestamp (t_0) dependence on ToT, the red curve is the 2nd-order polynomial fit that ultimately is used to correct t_0 . Both figures use a shaping time (ST) of 1 ns and correspond to a SNR of 30.

184 4. LGAD Front-end Electronics Performance

185 The FEE performance is studied as a function of irradiation for three different sce-
 186 narios: pre-radiation, and after neutron fluences of 5×10^{14} n/cm² and 1×10^{15} n/cm².
 187 We also quantify the effect of the BW of the FEE by varying the the ST (τ_s), four STs
 188 are considered: 0.5, 1, 2, and 4 ns. Additionally, we study the effect of noise by varying
 189 the SNR in all the scenarios described above. We consider three SNRs: 20, 30, and
 190 100. Sec. 4.1 summarizes the effects of the shaping time and SNR, and Sec. 4.2
 191 summarizes the effect of irradiation.

192 4.1. Front-end electronics shaping time and SNR studies

193 We scan the ST of the FEE and the SNR. The results for the pre-irradiated LGAD
 194 sensor are summarized in Table. 4.1, where the CF results are from the *ideal* implemen-
 195 tation. The *split-and-delay* and the *ideal* CFD implementations are compatible within
 196 uncertainties thus we only use one table for those results. We observe that the best
 197 results are consistently obtained by the 0.5 ns and 1.0 ns STs regardless of the SNR. We
 198 observe that longer STs are more affected by less favorable SNR. For example, for an
 199 SNR of 20, the time resolution is 37 ps and 100 ps for a ST of 0.5 ns and 4.0 ns, re-
 200 spectively. We note that CF consistently outperforms LE, and this effect is also observed

ST (ns)	Time Resolution (ps)			Constant Fraction		
	Leading Edge	SNR = 20	SNR = 30	SNR = 100	SNR = 20	SNR = 30
0.5	38.4 ± 2.1	34.9 ± 1.7	28.8 ± 1.0	37.2 ± 1.9	34.5 ± 1.6	29.8 ± 1.9
1.0	45.4 ± 2.2	37.3 ± 1.4	28.7 ± 1.7	36.4 ± 1.8	33.0 ± 1.4	25.9 ± 1.3
2.0	63.4 ± 2.5	47.6 ± 2.0	30.7 ± 1.2	47.6 ± 1.9	34.3 ± 1.6	28.7 ± 1.7
4.0	103.0 ± 4.1	75.3 ± 2.8	37.6 ± 2.0	73.8 ± 3.1	54.8 ± 2.1	32.1 ± 1.3

Table 2: $50\text{ }\mu\text{m}$ pre-radiation LGAD sensor simulation: summary of best time resolution obtained for SNRs of 20, 30, and 100. Leading edge and constant fraction results are shown.

ST (ns)	Time Resolution (ps)		
	$(RC)^2$	Constant Fraction	
2.0	$68.0 \pm xx$	$xx \pm xx$	$xx \pm xx$

Table 3: $50\text{ }\mu\text{m}$ pre-radiation LGAD sensor using a second order RC implementation of a CFD. Summary of best time resolution obtained using a ST of 2ns for SNRs of 20, 30, and 100.

for less favorable SNR and slower ST. Comparing CF and LE for the 1.0 ns ST with SNR of 20 yields a difference in performance of 26 ps, when subtracted in quadrature. Additionally, we observe that time resolutions better than 25 ps could not be achieved which is consistent with the known intrinsic jitter of the LGAD sensor. The latter is taken into account by the WF2 simulation and confirmed in our study. For a SNR of 1000 we obtained a time resolution consistent with 25 ps. Finally, in the case of the pre-irradiated sensor we observed that time resolutions of 35 ps are achievable for STs between 0.5 - 1.0 ns and a SNR of 30.

The **second order RC** CFD implementation shows a degradation on the time resolution when compared to the **split-and-delay**. Table. 4.1 shows the time resolution for the three SNR scenarios studied for a 2 ns ST. We observe a 50 ps degradation for a SNR of 20 and xx ps degradation for a SNR of 100.

4.2. Timing performance as a function of irradiation

We study the effect of irradiation on the time resolution of a $50\text{ }\mu\text{m}$ LGAD sensor. The impact of irradiation on the unprocessed signal pulse shapes are accounted for by

ST (ns)	Time Resolution (ps)			Constant Fraction		
	Leading Edge	SNR = 20	SNR = 30	SNR = 100	SNR = 20	SNR = 30
0.5	36.8 ± 1.9	32.0 ± 1.3	26.0 ± 1.2	32.5 ± 1.4	30.6 ± 1.2	25.1 ± 1.2
1.0	40.9 ± 1.4	33.8 ± 1.1	29.2 ± 1.0	33.4 ± 1.5	30.9 ± 0.9	26.1 ± 1.3
2.0	56.9 ± 2.4	45.3 ± 2.2	30.1 ± 1.1	43.7 ± 1.6	36.9 ± 1.3	24.4 ± 1.0
4.0	93.3 ± 3.6	67.9 ± 2.5	36.5 ± 1.3	70.8 ± 2.8	52.4 ± 1.9	29.9 ± 1.9

Table 4: $50\text{ }\mu\text{m}$ LGAD sensor simulation after neutron fluence of $5 \times 10^{14}\text{ n/cm}^2$: summary of best time resolution obtained for SNRs of 20, 30, and 100. Leading edge and constant fraction results are shown.

ST (ns)	Leading Edge			Time Resolution (ps)		
	SNR = 20	SNR = 30	SNR = 100	SNR = 20	SNR = 30	SNR = 100
0.5	47.8 ± 2.0	37.6 ± 2.0	26.6 ± 1.3	41.9 ± 1.9	34.3 ± 1.1	24.1 ± 1.0
1.0	59.9 ± 2.3	46.8 ± 1.8	28.1 ± 1.5	46.5 ± 1.9	36.8 ± 1.3	23.1 ± 0.9
2.0	89.7 ± 3.5	68.2 ± 2.6	32.3 ± 1.4	64.7 ± 2.8	49.6 ± 2.1	27.3 ± 0.9
4.0	147.3 ± 5.1	109.0 ± 4.3	42.6 ± 1.9	118.6 ± 4.0	84.1 ± 3.2	33.8 ± 1.1

Table 5: $50\text{ }\mu\text{m}$ LGAD sensor simulation after neutron fluence of $1 \times 10^{15}\text{ n/cm}^2$: summary of best time resolution obtained for SNRs of 20, 30, and 100. Leading edge and constant fraction results are shown.

the WF2 simulation. We consider three cases: pre-irradiated, and neutron fluences of $5 \times 10^{14}\text{ n/cm}^2$ and $1 \times 10^{15}\text{ n/cm}^2$. We perform the same studies as in the pre-irradiated case discussed in Sec. 4.1. The results for the irradiated LGAD are presented in Tab. 4.1 and Tab. 4.1 for neutron fluences of $5 \times 10^{14}\text{ n/cm}^2$ and $1 \times 10^{15}\text{ n/cm}^2$, respectively. We observe similar trends to those of the pre-radiation sensor described in Sec. 4.1. We note that when using STs between 0.5 - 1.0 ns and a SNR of 30, time resolutions of the order of 31 ps and 37 ps are obtained for $5 \times 10^{14}\text{ n/cm}^2$ and $1 \times 10^{15}\text{ n/cm}^2$, respectively.

5. Conclusion

We study the time resolution of a $50\text{ }\mu\text{m}$ Low-gain avalanche diode (LGAD) sensor using a simulation framework that includes the modeling of the raw unprocessed LGAD signal pulse, the front-end electronics, and effects of analog-to-digital converter resolution. We focus on the shaping time (ST) and signal-to-noise ratio (SNR) of the front-end electronics and its interplay with the irradiation level of the sensor. We reproduce the known LGAD jitter of 25 ps for fast STs and large SNRs. We observe a clear degradation of the time resolution with SNR and slower STs. The best results are obtained using a ST of 0.5 ns and using constant fraction (CF) discriminator, and similar results are obtained with a ST of 1.0 ns. For a SNR of 30 and for STs between 0.5-1.0 ns we obtain time resolutions between 30 - 37 ps for the 3 irradiations considered. The reduction in gain with irradiation could bring the SNR for the most irradiated LGAD ($1 \times 10^{15}\text{ n/cm}^2$) to 20 and thus worsen the time resolution to 42 - 47 ps. We note a clear gain in performance of CF over leading edge (LE) discriminators, particularly at low SNR and the largest irradiation level. For an ST of 1.0 ns at $\text{SNR} = 30$, the performance improvement of CF over LE is 26ps for the pre-irradiated sensor and 37ps for the irradiated sensor with neutron fluence of $1 \times 10^{15}\text{ n/cm}^2$. A performance degradation is observed when using a second order RC implementation of the CFD, especially at lower SNRs. Overall our simulation results indicate that time resolutions better than 45 ps are achievable for a $50\text{ }\mu\text{m}$ LGADs for irradiation levels up to neutron fluences of $1 \times 10^{15}\text{ n/cm}^2$.

Acknowledgment

A. Apresyan gratefully acknowledges support from DOE Early Career Research Program.

246 This document was prepared using the resources of the Fermi National Accelerator
247 Laboratory (Fermilab), a U.S. Department of Energy, Office of Science, HEP User Facility.
248 Fermilab is managed by Fermi Research Alliance, LLC (FRA), acting under Contract
249 No. DE-AC02-07CH11359. Part of this work was performed within the framework of
250 the CERN RD50 collaboration.

251 This work was supported by the Fermilab LDRD 2017.027 (**Cristian: did Artur ask**
252 **to include LDRD here?**); by the United States Department of Energy grant DE-FG02-
253 04ER41286; by the California Institute of Technology High Energy Physics under Con-
254 tract DE-SC0011925; by the European Union’s Horizon 2020 Research and Innovation
255 funding program, under Grant Agreement no. 654168 (AIDA-2020) and Grant Agree-
256 ment no. 669529 (ERC UFSD669529); by the Italian Ministero degli Affari Esteri and
257 INFN Gruppo V; and by the Spanish Ministry of Economy, Industry and Competitiveness
258 through the Particle Physics National Program (ref. FPA2014-55295-C3-2-R and
259 FPA2015-69260-C3-3-R) co-financed with FEDER funds.

260 **References**

- 261 [1] A. Apresyan, S. Xie, C. Pena, *et al.*, “Studies of Uniformity of 50 μm Low-Gain Avalanche Detectors
262 at the Fermilab Test Beam,” *Nucl. Instrum. Meth.*, vol. A895, pp. 158–172, 2018.
- 263 [2] N. Cartiglia *et al.*, “Beam test results of a 16 ps timing system based on ultra-fast silicon detectors,”
264 *Nucl. Instrum. Meth. A*, vol. 850, pp. 83 – 88, 2017.
- 265 [3] G. Pellegrini, P. Fernández-Martínez, M. Baselga, C. Fleta, D. Flores, V. Greco, S. Hidalgo,
266 I. Mandić, G. Kramberger, D. Quirion, and M. Ullan, “Technology developments and first mea-
267 surements of Low Gain Avalanche Detectors (LGAD) for high energy physics applications,” *Nuclear
268 Instruments and Methods in Physics Research Section A: Accelerators, Spectrometers, Detectors
269 and Associated Equipment*, vol. 765, pp. 12 – 16, 2014. HSTD-9 2013 - Proceedings of the 9th
270 International.
- 271 [4] H. F. W. Sadrozinski, A. Seiden, and N. Cartiglia, “4D tracking with ultra-fast silicon detectors,”
272 *Rept. Prog. Phys.*, vol. 81, no. 2, p. 026101, 2018.
- 273 [5] E. T. Whittaker, “Xviii.on the functions which are represented by the expansions of the interpolation-
274 theory,” *Proceedings of the Royal Society of Edinburgh*, vol. 35, p. 181194, 1915.
- 275 [6] C. E. Shannon, “A mathematical theory of communication,” *The Bell System Technical Journal*,
276 vol. 27, pp. 623–656, Oct 1948.